2026 IEEE/SICE International Symposium on System Integration (SII)
January 11-14, 2026. Cancún, México

Design, Modeling and Control of a Deformable Quadrotor Using McKibben Pneumatic Actuators

Keiichiro Kan[1], Junichiro Sugihara[1], Jinjie Li[1], Masaki Kitagawa[1], Kotaro Kaneko[2], and Moju Zhao[1]

***Abstract*— Deformable aerial robots with articulated structures have attracted increasing attention for their ability to perform complex tasks through in-flight morphological adaptation. However, most existing implementations rely on mechanical actuators, which increase total weight and vulnerability to external impacts. To address these limitations, we propose a deformable quadrotor platform actuated by antagonistic McKibben Pneumatic Actuators (MPAs), which offer lightweight, flexible, and robust actuation. We develop a dynamic model of the quadrotor incorporating joint angles actuated by MPAs, and characterize the relationship between internal pneumatic pressure and joint angle. Based on this model, we construct a prototype platform and evaluate its performance through a series of experiments. We first identify the optimal actuator length by analyzing joint deformation under varying pressure conditions. Next, we demonstrate stable flight during in-air morphing transitions, such as X-type, T-type, and H-type configurations, with position and attitude errors remaining within acceptable ranges. The results confirm that the proposed system enables stable flight using soft pneumatic actuation and paves the way for future aerial manipulation and morphing applications.**

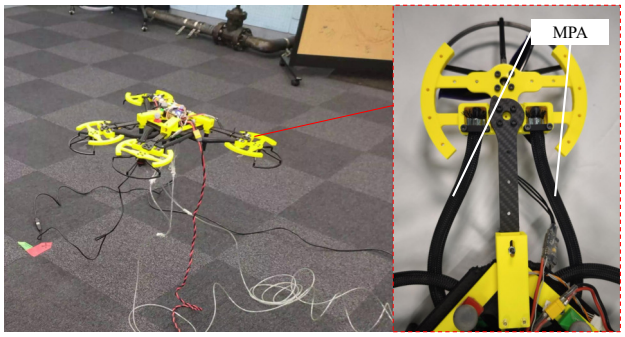

(a) Prototype of the deformable quadrotor.

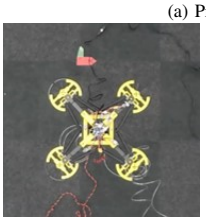

(b) X-type.

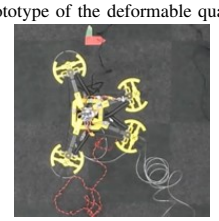

(c) T-type.

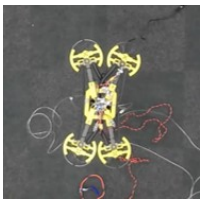

(d) H-type.

Fig. 1: Overview of the proposed deformable aerial robot. (a)the prototype platform actuated by antagonistic McKibben Pneumatic Actuators (MPAs). (b-d) Demonstration of morphing configurations: X-type, T-type, and H-type.

I. INTRODUCTION

In recent years, there has been increasing interest in aerial robots capable of executing complex tasks by exploiting their high degrees of freedom (DoF) in flight. Notably, deformable aerial robots equipped with articulated structures to enable both advanced flight performance and sophisticated manipulation have garnered significant attention [1]. A variety of such deformable aerial robots have been proposed to fulfill specific missions, such as navigating through confined environments [2, 3]. These robots typically achieve morphological transformation through the use of mechanical actuators such as motors. However, the implementation of these actuators tends to increase total weight when higher DoF are pursued, which can significantly impair flight performance. Furthermore, the added structural complexity often leads to reduced robustness against external impacts, thereby increasing the likelihood of damage upon physical contact with the environment.

To address these limitations, the use of flexible actuators has recently emerged as a promising alternative [4]. Among these, McKibben Pneumatic Actuators (MPAs) have been investigated as soft actuators exhibiting both flexibility and resilience. MPAs contract when pressurized with air and generate axial tensile force along their longitudinal axis. They are characterized by their lightweight structure, flexibility, and high power output [5]. These characteristics make them well-suited for deformable aerial robots that require both adaptability and robustness.

Nonetheless, pneumatic actuators are often criticized for requiring external hardware such as compressors or pressure tanks, which seemingly conflicts with the goal of lightweight aerial platforms. In this work, however, we challenge that assumption by reframing tethered pneumatic actuation not as a limitation but as a strategic advantage. Specifically, we focus on the emerging need for semi-autonomous or human-supervised aerial operations in indoor, constrained, or hazardous environments. Typical examples include factories, inspection tunnels, and caves, where tethered power or air supply is already feasible and desirable. Compared to electric actuators, pneumatic systems allow decoupling of the actuation unit from the power source, enabling high-output deformation while offloading heavy hardware to the ground. Furthermore, wired setups also eliminate flight-time constraints associated with battery capacity, thereby enhancing long-duration manipulation tasks.

[1]DRAGON Lab, Department of Mechanical Engineering, The University of Tokyo, Tokyo 113-8654, Japan kan, j-sugihara, jinjie-li, kitagawa, chou@dragon.t.u-tokyo.ac.jp
[2]HNL Lab, Department of Mechanical Engineering, The University of Tokyo, Tokyo 113-8654, Japan kaneko@hnl.t.u-tokyo.ac.jp

In this study, we propose and validate a novel deformable aerial robot equipped with antagonistic MPA pairs at each arm joint, enabling planar arm rotation through pressure differentials. This configuration supports multiple morphing modes including X-type, T-type, and H-type that can be dynamically selected during flight based on task demands as shown in Fig. 1.

We present a prototype design and modeling framework for the MPA-actuated platform and experimentally evaluate its performance. First, we analyze the relationship between MPA pressure and joint angle for different actuator lengths to determine the optimal configuration. Next, we conduct flight experiments to confirm the platform's ability to maintain stability during in-air morphing maneuvers.

II. Quadrotor with Antagonistic MPA Actuation Mechanism

A. Configuration of a Single MPA Unit

The McKibben Pneumatic Actuator (MPA) is a type of soft actuator that, while often driven by pneumatic pressure, can also utilize various types of fluids as its power source. To date, a wide range of fabrication methods for MPAs has been developed [6, 7]. A typical MPA consists primarily of a silicone tube encased within an external braided sleeve. When compressed air is supplied from an external compressor into the inner chamber, the actuator contracts along its longitudinal axis and simultaneously generates tensile force. Upon pressurization, the fiber angles within the braided sleeve increase, and this change in angle leads to axial contraction and the generation of tension.

MPAs have been explored as flexible actuators in a variety of systems [8], and numerous modeling approaches have been proposed to improve control performance by characterizing the actuator's input-output dynamics [5, 9]. Additionally, previous studies have investigated methods for achieving more flexible control over the structure and geometry of the braided fibers themselves [10, 11].

In this study, we fabricated MPAs based on a method proposed in prior work [6], which allows for lightweight construction and relatively simple assembly, as shown in Fig. 2. In Fig. 2, the upper MPA is in its unpressurized state, while the lower MPA is shown under applied pressure. The MPAs employed in this study consist of a silicone tube, a braided sleeve made of polyethylene terephthalate, hose clamps, straight fittings, and air plugs. The fibers used in the braided sleeve exhibit both flexibility and high tensile strength along the longitudinal direction. As a result, the fabricated MPA achieves variable stiffness, mechanical compliance, and lightweight characteristics suitable for actuator applications.

B. Antagonistic Actuation Mechanism with MPAs

While the MPAs employed in this study exhibit a high power-to-weight ratio, they generate linear motion and are thus commonly utilized in antagonistic actuation systems [12]. Fig. 3 illustrates the antagonistic actuation system used in this research. The ends of two MPAs are connected

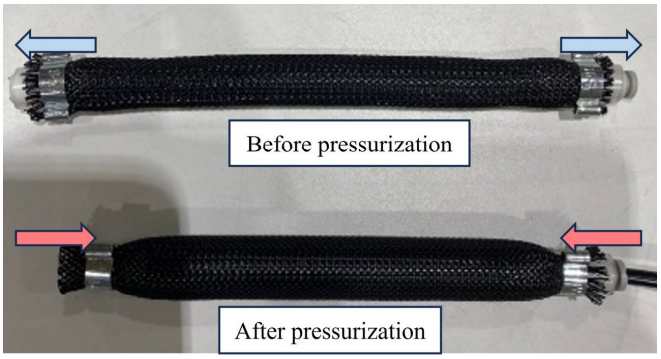

Fig. 2: McKibben Pneumatic Actuator.

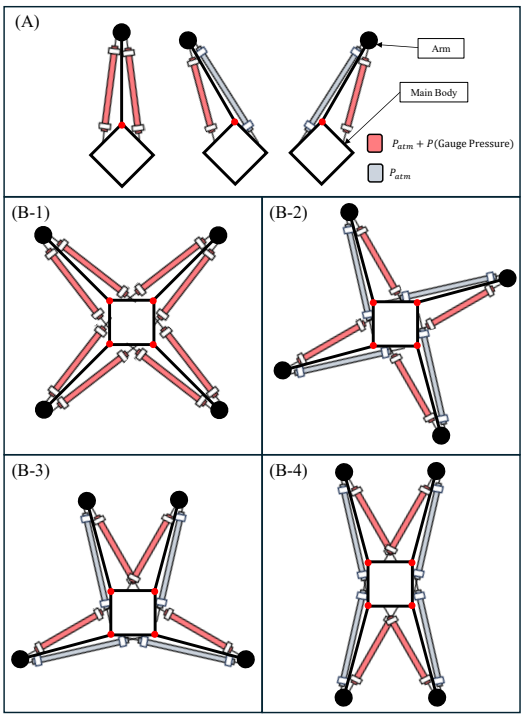

Fig. 3: Antagonistic actuation mechanism using McKibben Pneumatic Actuators (MPAs) and the resulting morphing configurations of the aerial robot. (A) Behavior of a single arm controlled by an antagonistic MPA pair. By generating a pressure difference between the two MPAs, the arm angle can be adjusted bidirectionally. (B-1) to (B-4): Morphing configurations achieved by coordinating all four arms. (B-1,2) Default (X-type) configuration. (B-3) T-type configuration. (B-4) H-type configuration.

respectively to the main body and the arm segment of the aerial robot. The internal pressure of each MPA is regulated independently using electro-pneumatic regulators. As illustrated in Fig. 3(A), applying differential pressure to a pair of MPAs results in antagonistic actuation, enabling three distinct behaviors: symmetric contraction, left-biased bending, and right-biased bending of a single joint. This mechanism allows each arm to be continuously and bidirectionally deformed, providing a foundation for achieving various morphing configurations of the entire aerial platform. Such shape-changing capabilities are reminiscent of work by Falanga et al. [13], which demonstrated multiple structural configurations using servo-driven folding mechanisms on

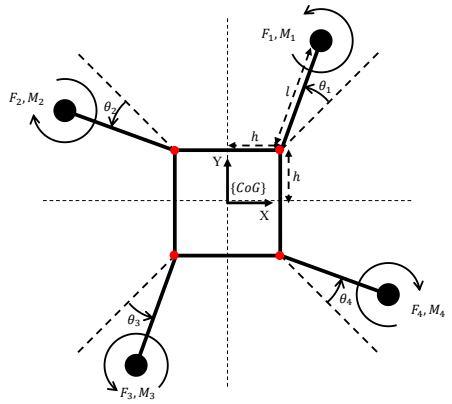

Fig. 4: Deformable Quadrotor Model.

drones. Similarly, our platform can achieve three distinct morphing configurations, labeled X-type, T-type, and H-type as shown in Fig. 3(B-1) through (B-4).

Each configuration offers advantages for specific aerial tasks:

- X-type (B-1,2) serves as the default mode and provides stable flight characteristics.
- T-type (B-3) configuration enables the arms to enclose or grasp objects positioned between them.
- H-type (B-4) narrows the lateral profile of the robot, making it suitable for navigating through narrow passages.

In this study, we primarily focus on validating the feasibility of the X, T, and H-type morphing configurations through physical experiments.

C. Scalability and Morphing DoF Analysis

The number of independent morphing degrees of freedom (DoF) achievable in an MPA-actuated aerial robot is intrinsically determined by the number of independent pneumatic pressure channels (i.e., air supply lines controlled by electro-pneumatic regulators). In the proposed system, each arm consists of an antagonistic pair of MPAs, which requires two independently regulated pressure sources to achieve bidirectional rotation. Therefore, the theoretical maximum number of independent joint DoF in a four-armed platform is four, which corresponds to eight MPAs and eight independent pressure channels (i.e., regulators). In this full-actuation scenario, each arm can be controlled independently, enabling arbitrary in-plane morphing configurations as shown conceptually in Fig. 3 (B-1)-(B-4). However, achieving such full actuation increases hardware complexity and weight due to the large number of regulators and associated valves. To address this, we explore reducing the number of pressure channels by grouping MPA pairs across arms to share the same pressure source. For example, using four pressure channels—one per actuator group—enables control of two independent morphing DoF. As shown in Fig. 3, the T-type, H-type, and X-type configurations can still be realized under this partial actuation scheme. In this study, we further reduce the number of pressure sources to two, yielding only a single morphing DoF. We experimentally validate two such configurations:

- X-T morphing with pressure groups assigned as in Fig. 3(B-1, B-3), and

- X-H morphing with pressure routing as in Fig. 3(B-1, B-4).

These configurations were implemented using the same prototype platform by simply switching the air inlet routing between tests. This flexible reassignment underscores the modular nature of pressure-based control and its suitability for adaptable morphing strategies.

Let n_a denote the number of arms (e.g., 4), and n_p the number of independent pressure channels available. Assuming each joint requires two actuators (antagonistic MPAs),the number of morphing degrees of freedom n_{DoF} is given by:

$$n_{\text{DoF}} = \min\left(n_a,\ \left\lfloor \frac{n_p}{2} \right\rfloor\right) \tag{1}$$

Conversely, if the pressure channels are shared across multiple joints, the effective n_{DoF} is reduced accordingly. In our study, $n_a = 4$, and we tested the cases $n_p = 2$ ($n_{\text{DoF}} = 1$). Under this constraint, we demonstrated flight with X-T and X-H morphing by switching air routing, validating the feasibility of simplified low-DoF designs.

III. Integration into Deformable Quadrotor Platform

A. Modeling And Control of Deformable Quadrotor

In this study, we implement the antagonistic actuation mechanism described in Section II-B on a quadrotor platform. The airframe is composed of a central body and four arms, each connected via 1-DoF revolute joint. These joints enable planar deformation of the arms, driven by antagonistic pairs of McKibben Pneumatic Actuators (MPAs). While the motion of the joints influences both the center of gravity (CoG) position and flight stability, we assume in this work that joint actuation occurs slowly relative to the flight dynamics. Under this quasi-static assumption, the joint angles θ_i can be incorporated into the model using forward kinematics, as similarly applied in the work of Zhao et al. [9].

The dynamic model of the deformable quadrotor is illustrated in Fig. 4. Each arm is actuated by a pair of MPAs that modulate the joint angle θ_i, thereby altering the spatial configuration of the rotors with respect to the body frame.

Let ${}^{\{\text{CoG}\}}\mathbf{r}_i = [\,{}^{\{\text{CoG}\}}r_{x_i},\ {}^{\{\text{CoG}\}}r_{y_i}\,]^T$ denote the vector from the CoG frame to the i-th rotor. In the 2D planar configuration, the position vectors from the CoG to each rotor are defined as:

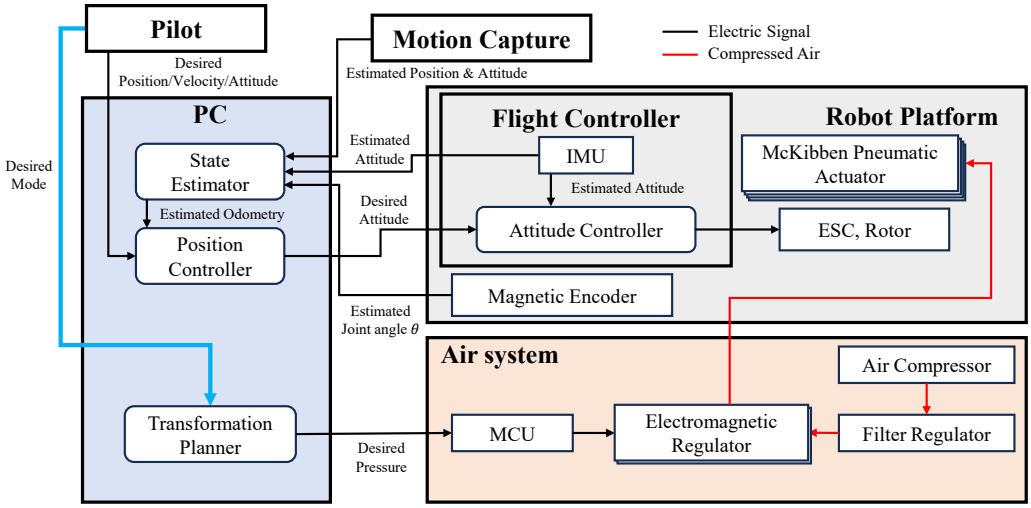

Fig. 5: System Architecture of the aerial robot.

$$\begin{pmatrix} {}^{\{\mathrm{CoG}\}}r_{x_i} \\ {}^{\{\mathrm{CoG}\}}r_{y_i} \end{pmatrix} = \begin{cases} \begin{pmatrix} h + l\cos\left(\theta_1 + \frac{\pi}{4}\right) \\ h + l\sin\left(\theta_1 + \frac{\pi}{4}\right) \end{pmatrix}, & i = 1 \\ \begin{pmatrix} -h - l\sin\left(\theta_2 + \frac{\pi}{4}\right) \\ h + l\cos\left(\theta_2 + \frac{\pi}{4}\right) \end{pmatrix}, & i = 2 \\ \begin{pmatrix} -h - l\cos\left(\theta_3 + \frac{\pi}{4}\right) \\ -h - l\sin\left(\theta_3 + \frac{\pi}{4}\right) \end{pmatrix}, & i = 3 \\ \begin{pmatrix} h + l\sin\left(\theta_4 + \frac{\pi}{4}\right) \\ -h - l\cos\left(\theta_4 + \frac{\pi}{4}\right) \end{pmatrix}, & i = 4 \end{cases} \tag{2}$$

The thrust force and drag torque generated by each propeller are denoted as F_i and M_i, respectively. According to a standard motor model, there exists a linear relationship between the generated thrust and its corresponding torque:

$$M_i = c_i F_i, \quad c_i = (-1)^i c, \tag{3}$$

where c is a positive constant, and c_i captures the direction of rotor spin: odd-numbered rotors ($i = 1, 3$) rotate counter-clockwise (CCW), while even-numbered rotors ($i = 2, 4$) rotate clockwise (CW).

The translational and rotational dynamics of the deformable quadrotor in the world frame $\{W\}$ and CoG frame $\{\mathrm{CoG}\}$ are expressed as follows:

$$M\,{}^{\{W\}}\ddot{\mathbf{r}} = {}^{\{W\}}R_{\{\mathrm{CoG}\}} \begin{bmatrix} 0 \\ 0 \\ \sum_{i=1}^{4} F_i \end{bmatrix} + \begin{bmatrix} 0 \\ 0 \\ -Mg \end{bmatrix}, \tag{4}$$

$${}^{\{\mathrm{CoG}\}}I^{\{\mathrm{CoG}\}}\,\dot{\boldsymbol{\omega}} = \begin{bmatrix} \sum_{i=1}^{4} {}^{\{\mathrm{CoG}\}}r_{y_i}(\theta_i)\,F_i \\ -\sum_{i=1}^{4} {}^{\{\mathrm{CoG}\}}r_{x_i}(\theta_i)\,F_i \\ \sum_{i=1}^{4} c_i\,F_i \end{bmatrix} - {}^{\{\mathrm{CoG}\}}\boldsymbol{\omega} \times \left({}^{\{\mathrm{CoG}\}}I^{\{\mathrm{CoG}\}}\boldsymbol{\omega}\right), \tag{5}$$

where ${}^{\{W\}}\mathbf{r}$ is the position of the CoG frame expressed in the world frame $\{W\}$, and ${}^{\{\mathrm{CoG}\}}\boldsymbol{\omega} = \left[{}^{\{\mathrm{CoG}\}}\omega_x,\ {}^{\{\mathrm{CoG}\}}\omega_y,\ {}^{\{\mathrm{CoG}\}}\omega_z\right]^{\mathrm{T}}$ denotes the angular velocity of the single body system with respect to the world frame, expressed in the $\{\mathrm{CoG}\}$ frame. This dynamic model serves as the foundation for the control strategy adopted in this study, which is based on the method developed by Zhao et al. [14]. In addition, regarding flight stability during morphing, we directly inject the measured joint angles θ_i from the joint sensors into the geometric model used for per-rotor thrust allocation. Thus, attitude stabilization is referenced to the current geometry, rather than to a nominal predeformation layout. Under a quasi-static process, we perform morphing slowly during flight. As described in Section II-B, for the T and H-type transformations we recompute the per rotor position vectors ${}^{\{\mathrm{CoG}\}}\mathbf{r}_i$ based on the measured joint angles θ_i in real time. This approach allows us to maintain stable flight during in-air morphing maneuvers.

B. System Architecture

An overview of the proposed system architecture is illustrated in Fig. 5. The deformable aerial robot integrates two major subsystems: an electric system and a pneumatic actuation system. All primary components - including sensors, flight controller, and pressure regulation modules - are interconnected via the Robot Operating System (ROS) framework, which provides a standardized communication interface. Compressed air is generated by an external compressor unit and regulated using electro-pneumatic regulators. Through flexible tubing, the pressurized air is delivered to the McKibben Pneumatic Actuators (MPAs) embedded in the aerial platform. By adjusting the internal pressure of each MPA in real time, this system enables in-flight structural morphing of the quadrotor.

IV. Experiment

In this section, we describe the hardware configuration of the proposed aerial robot, evaluate its deformation behavior

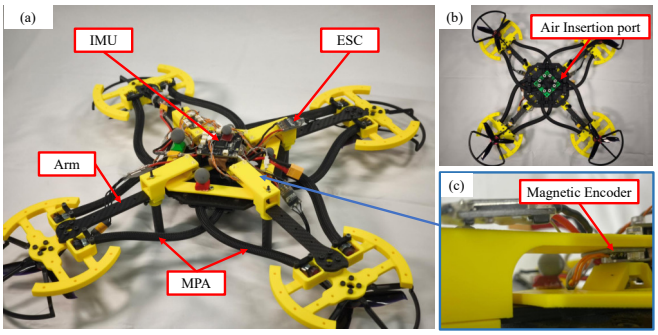

Fig. 6: (a) : Robot prototype platform with McKibben Pneumatic Actuators (MPAs). (b) : Rear view of the robot, showing the air insertion port. (c) : Close-up view of the joint section, showing the magnetic encoder for measuring the joint angle.

TABLE I: Specifications of the Deformable Quadrotor Platform

Attribute	Value
rotor KV	2300 RPM/V
mass	0.963 kg
Supply voltage	15.0 V
size	0.490 × 0.490 × 0.115 m

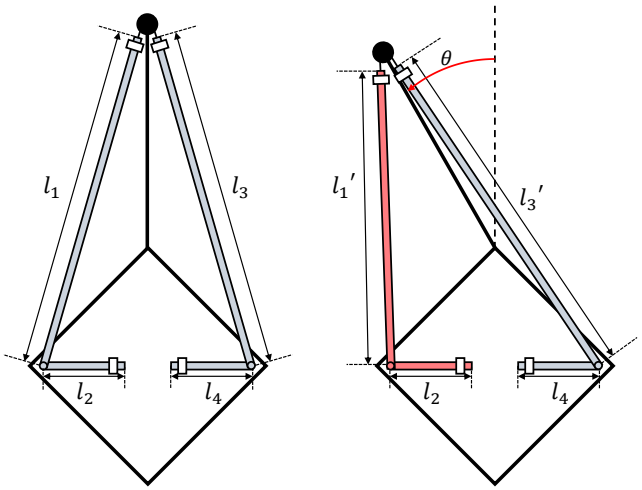

Fig. 7: Geometric model of joint rotation induced by antagonistic MPA contraction. Left: Initial undeformed configuration, where l_1 and l_3 represent the actuator lengths and l_2, l_4 denote horizontal mounting offsets. Right: Deformed state due to actuation, with resulting contraction lengths l_1', l_3' and generated joint angle θ.

induced by pneumatic actuation, and finally validate its flight performance through experiments under different morphing modes.

A. Robot Platform

The prototype of the deformable aerial robot developed in this study is shown in Fig. 6, and its key specifications are listed in Table I. As shown in Fig. 6(a), the platform consists of a central body and four arms, each connected via a single revolute joint. Each arm is equipped with a rotor and its corresponding electronic speed controller (ESC), along with a pair of McKibben Pneumatic Actuators (MPAs) for antagonistic actuation. To ensure structural rigidity where required, Carbon Fiber Reinforced Polymer (CFRP) plates are used for specific sections of the arms, while the remainder of the structure - including the body and arm mounts - is fabricated using 3D-printed PLA components. Fig. 6(b) shows the rear view of the robot, where pneumatic air insertion ports are located. These are used to inject compressed air into the MPAs. In addition, Fig. 6(c) illustrates the magnetic rotary encoder (AS5600 Breakout Board) used to measure the joint rotation angle θ_i. In the experimental setup, the internal pressure applied to each MPA is controlled via an electro-pneumatic regulator (ITV1050-212BS).

B. Joint Angle Characterization with Varying MPA Lengths

In this section, we experimentally evaluate the relationship between air pressure applied to antagonistically arranged MPAs and the resulting joint rotation angle. Each joint of the proposed deformable aerial robot is actuated by a pair of McKibben Pneumatic Actuators (MPAs), forming a one degree of freedom (1-DoF) rotational mechanism. These MPAs are attached between the main body and the arm, and generate torque through axial contraction when pressurized.

The joint angle θ depends not only on the pressure difference between the two actuators (P_1 and P_2), but also on the geometric configuration of the actuator mounting positions, including their initial lengths. As illustrated in Fig. 7, both the actuator contraction length components (l_1, l_3) and the mounting offsets (l_2, l_4) play critical roles in determining the initial actuator length and torque arm, thereby affecting the rotational behavior.

Therefore, the joint angle can be modeled as a function of both pressure inputs and geometric parameters as:

$$\theta = \theta(P_1, P_2) = \theta(l_1, l_2, l_3, l_4) \tag{6}$$

In particular, the maximum joint angle can be approximated as:

$$\theta_{\max} = \theta(l_{1,\min}, l_{3,\max}) \tag{7}$$

In this experiment, we investigate the influence of varying MPA lengths on the achievable joint angles, aiming to determine the optimal actuator configuration for the deformable aerial platform. To quantitatively evaluate the relationship between joint angle θ and pressure, we prepared five sets of antagonistic MPA pairs with different initial lengths: 0.240 m, 0.245 m, 0.250 m, 0.255 m, and 0.260 m. All MPAs used in the experiment shared the same inner diameter and braided mesh structure, with only the initial length being varied.

In each experiment, one of the MPAs was held at a fixed pressure (R-fixed or L-fixed), while the opposing actuator was pressurized step-by-step from 0 to 0.7 MPa. For example, we first fixed the right-side actuator (R-pressure) and increased the left-side pressure (L-pressure), then repeated the test by swapping the pressure roles. Although the antagonistic MPA configuration is theoretically symmetric, this approach allowed us to examine possible hysteresis, actuator asymmetry, or mounting-related deviations in real-world conditions. The joint angle θ was measured using a magnetic rotary encoder (AS5600 Breakout Board) mounted

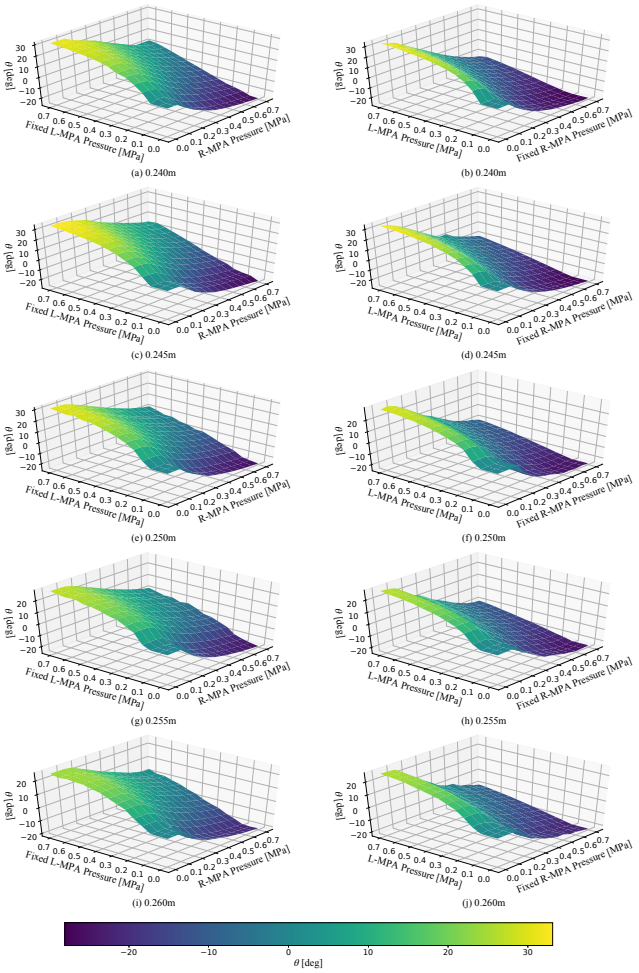

Fig. 8: Experimental results of joint angle θ in response to varying pressure input across different MPA lengths. Each row shows measurements for a different MPA length.

TABLE II: Minimum and maximum joint angles achieved for different MPA lengths

MPA Lengths[m]	$\theta_{\min}$[deg]	$\theta_{\max}$[deg]
0.240	-26.54	32.79
0.245	-28.04	33.11
0.250	-25.66	30.76
0.255	-25.14	27.69
0.260	-22.41	26.01

at the joint axis. The encoder detected the magnetic field orientation of a permanent magnet attached to the axis.

The experimental results for the joint angle measurements are presented in Fig. 8. Each subfigure corresponds to a different MPA length: (a) and (b) for 0.240 m, (c) and (d) for 0.245 m, (e) and (f) for 0.250 m, (g) and (h) for 0.255 m, and (i) and (j) for 0.260 m. For each length, the left subfigure shows the results under R-fixed and L-pressurized conditions, and the right subfigure shows L-fixed and R-pressurized. In general, shorter MPAs yielded limited angular range due to insufficient contraction stroke, while overly long MPAs showed restricted deformation due to structural interference with the joint geometry. Among all tested lengths as shown in Table II, the 0.245 m MPA configuration exhibited the best

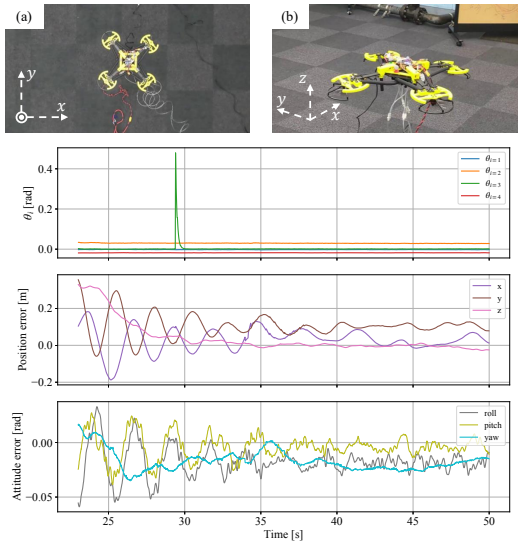

Fig. 9: X-type experiment. (a) Top view of a quadrotor. (b) Side view of a quadrotor. The lower plots show: (Top): Time-series of joint angles θ_i for each arm. (Middle): Position errors in the x, y, and z directions. (Bottom): Attitude errors in roll, pitch, and yaw. These results demonstrate stable flight performance during and after the X-type shape transition.

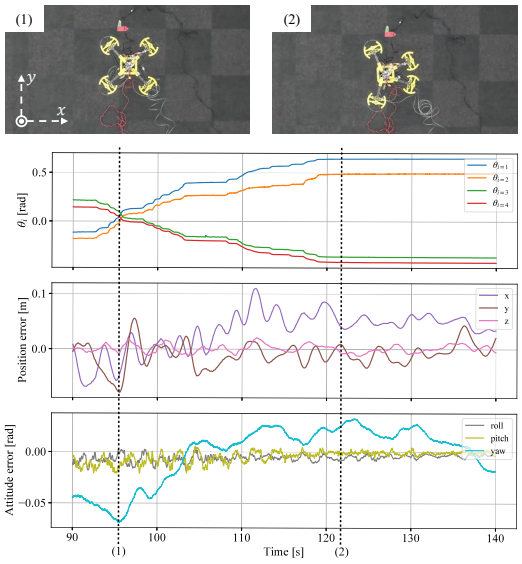

Fig. 10: T-type morphing experiment. (1) Before deformation; (2) After deformation. The lower plots show: (Top): Time-series of joint angles θ_i for each arm. (Middle): Position errors in the x, y, and z directions. (Bottom): Attitude errors in roll, pitch, and yaw. These results demonstrate stable flight performance during and after the T-type shape transition.

performance in terms of both symmetry and angular range. It achieved a rotation from $-28.04°$ to $+33.11°$, which is considered sufficient to support meaningful morphological transitions during flight.

The differences between the two pressurization directions (R-fixed vs. L-fixed) were minor, suggesting that the MPAs and mounting structure were sufficiently symmetric. Some hysteresis or asymmetry was observed, but its impact on control performance is negligible. Based on these findings, we selected the 0.245 m MPAs as the optimal actuator length

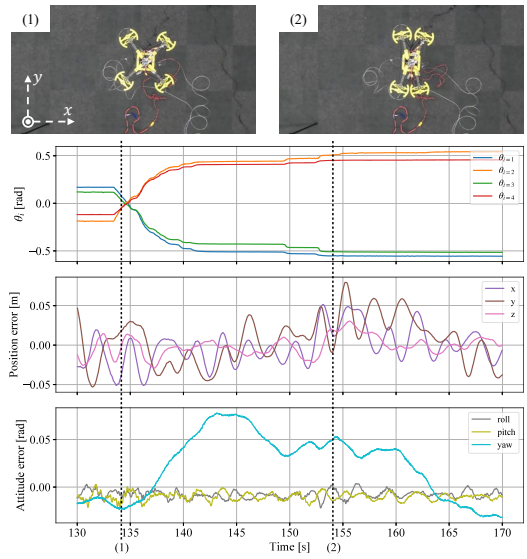

Fig. 11: H-type morphing experiment. (1) Before deformation; (2) After deformation. The lower plots show: Top: Time-series of joint angles θ_i for each arm. Middle: Position errors in the x, y, and z directions. Bottom: Attitude errors in roll, pitch, and yaw. These results demonstrate stable flight performance during and after the H-type shape transition.

for the deformable aerial robot platform used in this study.

C. Evaluation of Flight Stability Under Morphing Conditions

Based on the robot configuration selected in the previous section, we conducted flight experiments to evaluate stability during in-flight structural morphing. Specifically, we tested three morphing patterns X, T, and H-type as defined in Section II-B while the robot maintained a hovering state. The X-type serves as the fundamental and initial configuration of the robot, from which other morphologies are generated. Notably, the transitions between X and T, as well as X and H, are reversible under antagonistic actuation. In contrast, as described in the previous section, the H-type configuration does not allow reversible transformation from or to the T-type due to mechanical constraints. During each experiment, we commanded the platform to hover in place and then applied morphing commands to transition into the T or H-type configurations using antagonistic actuation. The deformation angles of each arm, as well as the resulting deviations in position and attitude, were recorded using the onboard IMU and motion capture system.

We first evaluated the flight stability in the baseline X-type configuration. The results, shown in Fig. 9, include time-series plots of joint angles, position errors, and attitude errors. The RMS of the errors in this case were:

- RMS of position errors: [0.0635, 0.1174, 0.0491] m
- RMS of attitude errors: [0.0437, 0.0236, 0.0145] rad

Next, we examined the T-type morphing, with results shown in Fig. 10. The RMS of errors during and after morphing were:

- RMS of position errors: [0.0382, 0.0221, 0.0420] m
- RMS of attitude errors: [0.0116, 0.0152, 0.0478] rad

Similarly, Fig. 11 presents the results for H-type morphing:

- RMS of position errors: [0.0214, 0.0441, 0.0602] m
- RMS of attitude errors: [0.0241, 0.0086, 0.0896] rad

In all three morphing cases, the RMS of position errors remained consistently low throughout the morphing process, indicating that stable flight was successfully maintained during and after the deformation. The T-type configuration exhibited minimal disturbance in both position and attitude, confirming the system's robustness even during transition. By contrast, H-type morphing introduced relatively larger yaw errors, likely due to the elongated structure causing a thrust imbalance among the rotors. These experiments validate that the proposed system supports morphing across multiple configurations while maintaining flight stability. Furthermore, the flexibility of reversible transitions between X, T, and H shapes lays the groundwork for practical aerial applications such as navigation in cluttered spaces, aerial interaction, and adaptive manipulation. Nonetheless, challenges remain, such as morphing-induced disturbances, actuation latency, and mechanical hysteresis, which necessitate further work on actuator modeling, control refinement, and hardware optimization. As future work, we will relax the current morphing-DoF constraint and investigate geometry-aware controllers.

V. CONCLUSIONS

In this study, we presented the design, modeling, and experimental validation of a deformable quadrotor platform actuated by antagonistic McKibben Pneumatic Actuators (MPAs). We first developed a dynamic model of the aerial robot with revolute joints at each arm, enabling in-plane structural morphing. The antagonistic actuation mechanism allowed each arm to rotate bidirectionally by modulating internal air pressure, and we characterized the relationship between MPA pressure and joint angle to guide hardware selection.

Using the selected actuator configuration, we conducted flight experiments to evaluate the stability of the robot under different morphing conditions. The T-type and H-type configurations demonstrated the system's robustness in maintaining stable flight during structural morphing, with RMS position errors kept consistently low in both cases.

Overall, the proposed system provides a lightweight, impact-resilient, and morphologically adaptable solution for future aerial robotic applications. In future work, we plan to develop an optimized design that supports a wider range of morphing configurations, allowing for greater adaptability in various aerial tasks. Additionally, we aim to establish control strategies that actively leverage structural deformation for task execution, such as grasping, navigation in confined spaces, or mid-air manipulation.

REFERENCES

[1] A. Ollero, M. Tognon, A. Suarez, D. Lee, and A. Franchi, "Past, present, and future of aerial robotic manipulators," *IEEE Transactions on Robotics*, vol. 38, no. 1, pp. 626–645, 2022.

[2] N. Zhao, Y. Luo, H. Deng, and Y. Shen, "The deformable quad-rotor: Design, kinematics and dynamics characterization, and flight performance validation," in *2017 IEEE/RSJ International Conference on Intelligent Robots and Systems (IROS)*, 2017, pp. 2391–2396.

[3] M. Zhao, K. Kawasaki, K. Okada, and M. Inaba, "Transformable multirotor with two-dimensional multilinks: modeling, control, and motion planning for aerial transformation," *Advanced Robotics*, vol. 30, no. 13, pp. 825–845, 2016.

[4] A. E. Gomez-Tamm, P. Ramon-Soria, B. Arrue, and A. Ollero, "Current state and trends on bioinspired actuators for aerial manipulation," in *2019 Workshop on Research, Education and Development of Unmanned Aerial Systems (RED UAS)*, 2019, pp. 352–361.

[5] B. Tondu and P. Lopez, "Modeling and control of mckibben artificial muscle robot actuators," *IEEE Control Systems Magazine*, vol. 20, no. 2, pp. 15–38, 2000.

[6] K. Naniwa, Y. Masuda, D. Nakanishi, D. Ura, and Y. Sugimoto, "A musculoskeletal robot tool kit," *JSME annual Conference on Robotics and Mechatronics (Robomec)*, vol. 2022, pp. 2A2–M08, 2022.

[7] T. Takuma, "Legged robot driven by soft pneumatic actuators," *Journal of the Robotics Society of Japan*, vol. 37, no. 2, pp. 144–149, 2019.

[8] M. A. M. Dzahir and S.-i. Yamamoto, "Recent trends in lower-limb robotic rehabilitation orthosis: Control scheme and strategy for pneumatic muscle actuated gait trainers," *Robotics*, vol. 3, no. 2, pp. 120–148, 2014.

[9] C.-P. Chou and B. Hannaford, "Measurement and modeling of mckibben pneumatic artificial muscles," *IEEE Transactions on Robotics and Automation*, vol. 12, no. 1, pp. 90–102, 1996.

[10] K. Takashima, J. Rossiter, and T. Mukai, "Mckibben artificial muscle using shape-memory polymer," *Sensors and Actuators A: Physical*, vol. 164, no. 1, pp. 116–124, 2010.

[11] D. Sangian, A. Jeiranikhameneh, S. Naficy, S. Beirne, and G. Spinks, "Three-dimensional printed braided sleeves for manufacturing mckibben artificial muscles," *3D Printing and Additive Manufacturing*, vol. 6, 2018.

[12] B.-S. Kang, C. S. Kothera, B. K. S. Woods, and N. M. Wereley, "Dynamic modeling of mckibben pneumatic artificial muscles for antagonistic actuation," in *2009 IEEE International Conference on Robotics and Automation*, 2009, pp. 182–187.

[13] D. Falanga, K. Kleber, S. Mintchev, D. Floreano, and D. Scaramuzza, "The foldable drone: A morphing quadrotor that can squeeze and fly," *IEEE Robotics and Automation Letters*, vol. 4, no. 2, pp. 209–216, 2019.

[14] M. Zhao, T. Anzai, F. Shi, T. Maki, T. Nishio, K. Ito, N. Kuromiya, K. Okada, and M. Inaba, "Versatile multilinked aerial robot with tilted propellers: Design, modeling, control, and state estimation for autonomous flight and manipulation," *Journal of Field Robotics*, vol. 38, no. 7, pp. 933–966, 2021.